nature nanotechnology

ARTICLES

https://doi.org/10.1038/s41565-018-0183-2

Corrected: Author Correction

Non-flammable electrolyte enables Li-metal batteries with aggressive cathode chemistries

Xiulin Fan[1,5], Long Chen[1,5], Oleg Borodin[2], Xiao Ji[1], Ji Chen[1], Singyuk Hou[1], Tao Deng[1], Jing Zheng[1], Chongyin Yang[1], Sz-Chian Liou[3], Khalil Amine[4]*, Kang Xu[2]* and Chunsheng Wang[1]*

Rechargeable Li-metal batteries using high-voltage cathodes can deliver the highest possible energy densities among all electrochemistries. However, the notorious reactivity of metallic lithium as well as the catalytic nature of high-voltage cathode materials largely prevents their practical application. Here, we report a non-flammable fluorinated electrolyte that supports the most aggressive and high-voltage cathodes in a Li-metal battery. Our battery shows high cycling stability, as evidenced by the efficiencies for Li-metal plating/stripping (99.2%) for a 5 V cathode $LiCoPO_4$ (~99.81%) and a Ni-rich $LiNi_{0.8}Mn_{0.1}Co_{0.1}O_2$ cathode (~99.93%). At a loading of 2.0 mAh cm^{-2}, our full cells retain ~93% of their original capacities after 1,000 cycles. Surface analyses and quantum chemistry calculations show that stabilization of these aggressive chemistries at extreme potentials is due to the formation of a several-nanometre-thick fluorinated interphase.

The energy density of lithium-ion batteries (LIBs)[1–3] has gradually approached the upper limit of capacity allowed by intercalation chemistry (300 Wh kg^{-1})[4,5]. Increasing the capacity of LIBs to 500 Wh kg^{-1}, a new goal set by automotive applications for a longer driving range with a single charge, will have to resort to more aggressive chemistries such as conversion-reaction or high-voltage/high-capacity intercalation cathodes, all of which involve Li metal as the anode.

Li metal offers one of the highest specific capacities (3,860 mAh g^{-1}) and the lowest redox potential (−3.04 V versus standard hydrogen electrode (SHE))[6,7]. Its coupling with a high-voltage/high-capacity cathode such as $LiNi_{0.8}Mn_{0.1}Co_{0.1}O_2$ (NMC811) or $LiCoPO_4$ (LCP) would create a high-energy density cell that meets the 500 Wh kg^{-1} goal[4]. However, numerous fundamental challenges, arising from the highly reactive nature of both the Li-metal anode and these aggressive cathodes, preclude the practical realization of rechargeable Li-metal batteries (LMBs). Because of their high reactivity, LMBs constantly operate with low Coulombic efficiency, signalling the rapid consumption of both electrolyte and Li and leading to a short cycle life. Though the instantaneous reactions between electrolytes and Li create a passivation layer called the solid electrolyte interphase (SEI), its inhomogeneous composition and morphology induce Li dendritic growth, which compromises LMB cycle life and safety[8–14]. On the cathode side, electrolyte oxidation leads to a cathode electrolyte interphase (CEI)[15], which at high voltage does not sufficiently stabilize the electrolyte from sustained oxidation.

Early investigations of LMBs focused on ether-based electrolytes due to their lower reactivity with Li metal (Coulombic efficiency of ~95–99%)[12,13,15–17], but ethers are generally unstable towards oxidation (<4.0 V versus Li^+/Li, Supplementary Fig. 1) and extremely flammable (Supplementary Video 1). Carbonate electrolytes show high oxidation potential (4.3 V) and have been successfully used in commercial LIBs, but the intrinsic reactivity of their carbonyl functionality towards Li metal confines the Li plating/stripping Coulombic efficiency to below 90%, accompanied by Li dendrite growth[6,18]. Furthermore, in the presence of aggressive cathodes such as 4.4 V NMC811 or 5.0 V LCP, the carbonate-based electrolytes become anodically unstable, with the thermodynamic tendency of releasing CO_2 and O_2. Thus, though cells constructed with Li||NMC811 and Li||LCP provide desirable energy densities, they are typically characterized by a low Coulombic efficiency[19,20] and rapid capacity fade[19–24]. To counter this issue, highly concentrated electrolytes have been used, substantially improving the reported stability[16,25–27]. However, the extremely high salt concentration considerably raises not only the cost but also electrolyte viscosity. The latter causes low wettability for both the electrodes and the separator, leading to poor rate performances and under-utilization of active materials.

Here, we report a non-flammable electrolyte that demonstrates excellent stability toward both a Li-metal anode and high-voltage/high-capacity cathodes. It consists of 1 M lithium hexafluorophosphate ($LiPF_6$) in a mixture of fluoroethylene carbonate/3,3,3-fluoroethylmethyl carbonate/1,1,2,2-tetrafluoroethyl-2′,2′,2′-trifluoroethyl ether (FEC:FEMC:HFE, 2:6:2 by weight). Unlike the previously reported fluorinated electrolytes, which suffered from increasing impedance at the anode side[28,29], this all-fluorinated electrolyte enables a high Li plating/stripping Coulombic efficiency of 99.2% and suppresses dendrites without raising the interfacial impedance. It also supports the stable cycling of NMC811 (Coulombic efficiency of ~99.93%) and LCP (Coulombic efficiency of ~99.81%) cathodes by forming a highly fluorinated interphase with thickness of 5–10 nm that is responsible for the effective inhibition of electrolyte oxidation and transition metal dissolution. Unprecedented cycling stabilities were obtained for both Li||NMC811 (90% retention at the 450th cycle) and Li||LCP cells (93% retention at the 1,000th cycle).

Electrochemical stability of all-fluorinated electrolyte

The Li-metal cycling stability in this all-fluorinated electrolyte was demonstrated using a Li-free configuration coin cell (Li||Cu) (Fig. 1a–c). Clearly, the all-fluorinated electrolyte generates lower

---

[1]Department of Chemical and Biomolecular Engineering, University of Maryland, College Park, MD, USA. [2]Electrochemistry Branch, Power and Energy Division Sensor and Electron Devices Directorate, US Army Research Laboratory, Adelphi, MD, USA. [3]Maryland Nanocenter, University of Maryland, College Park, MD, USA. [4]Chemical Sciences and Engineering Division, Argonne National Laboratory, Argonne, IL, USA. [5]These authors contributed equally: Xiulin Fan, Long Chen. *e-mail: amine@anl.gov; conrad.k.xu.civ@mail.mil; cswang@umd.edu

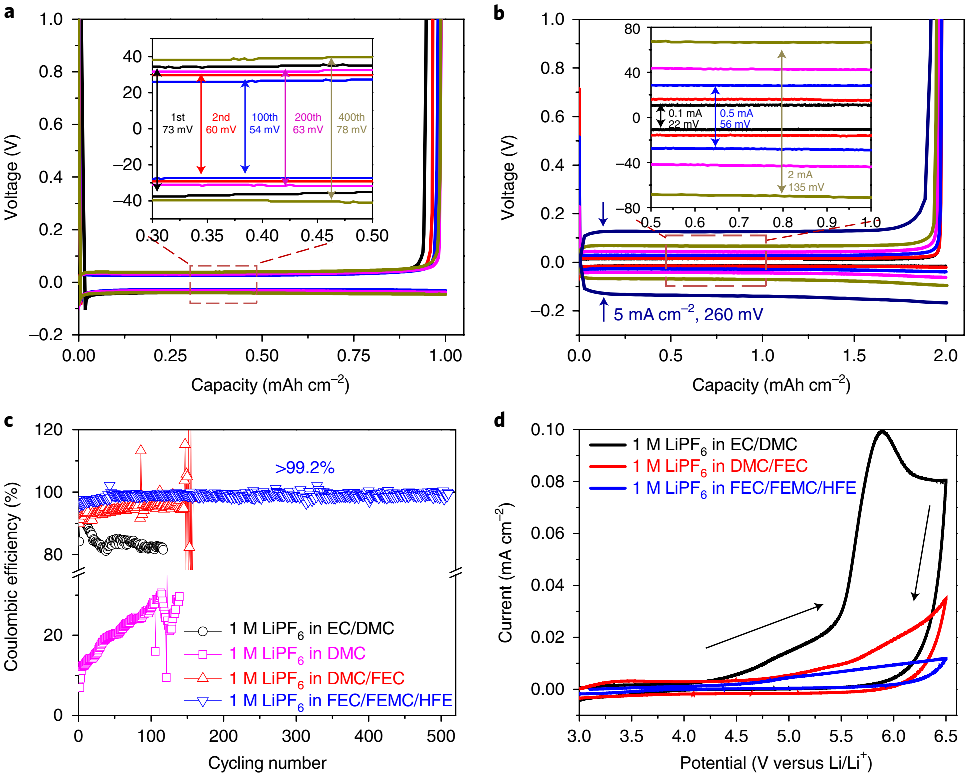

Fig. 1 | Electrochemical properties for different electrolytes. a, Li-metal plating/stripping profiles on a Cu working electrode cycled in 1 M LiPF$_6$ in our electrolyte (FEC:FEMC:HFE = 2:6:2) at a current density of 0.5 mA cm^{-2}. **b**, Polarization profiles for Li plating/stripping in 1 M LiPF$_6$ FEC/FEMC/HFE at different current densities. **c**, Li plating/stripping Coulombic efficiency in different electrolytes at 0.2 mA cm^{-2}. Capacity: 1 mAh cm^{-2}. **d**, Oxidation stabilities for different electrolytes as evaluated on stainless steel electrodes at a scanning rate of 5 mV s^{-1}.

overpotentials (Fig. 1a) than conventional carbonate and FEC-based electrolytes (Supplementary Fig. 2), though its conductivity (5.1 mS cm^{-1}) is lower than that of ethylene carbonate/dimethyl carbonate (EC/DMC) or FEC/DMC (10.7 and 10.3 mS cm^{-1}, respectively) (Supplementary Fig. 3). The polarization for the Li plating/stripping process increases with current density (Fig. 1b), reaching 130 mV at a current density of 5 mA cm^{-2}, which is comparable to that observed in concentrated ether electrolyte[16], but lower than for 7 M LiFSI–FEC electrolyte[26]. The exchange current density estimated from Tafel plots further confirmed facile Li plating/stripping (Supplementary Fig. 4). The all-fluorinated electrolyte also significantly enhanced the Li stripping/plating Coulombic efficiency and cycling stability. At 0.2 mA cm^{-2}, the Li plating/stripping Coulombic efficiency in the all-fluorinated electrolyte increases to >99.2% within 50 cycles (Fig. 1c). As current density and Li turnover levels reach 0.5 mA cm^{-2} and 2.0 mAh cm^{-2}, the Coulombic efficiency remains at ~99% after the initial activation cycles (Supplementary Fig. 5). In contrast, DMC, EC/DMC, a carbonate–ether mixture and FEC/DMC demonstrate Coulombic efficiencies of ~20, ~80, 60–85 (Supplementary Fig. 6) and 95%, respectively. As a result of the high reversibility, remarkable cycling stability and stable Li plating/stripping potentials were demonstrated by the all-fluorinated electrolyte for over 500 cycles (Fig. 1c).

The oxidation stability of various electrolytes was evaluated using cyclic voltammetry (CV) on stainless steel electrodes. Ether-based electrolyte, even at a high salt concentration (4 M), shows little stability against oxidation, as evidenced by a rapid increase in current above 4.0 V (Supplementary Fig. 1), while all other electrolytes remain stable. Among these electrolytes (Fig. 1d), the conventional EC/DMC formulation exhibits anodic decomposition above 4.3 V. The oxidation stability is improved after FEC replaces EC; however, a high anodic current is still observed at ~5.0 V, indicating an irreversible and sustained oxidation. In contrast, low anodic current was observed even at 6.5 V for the all-fluorinated electrolyte. A more aggressive floating test further confirmed this high anodic stability (Supplementary Fig. 7). Overall, the all-fluorinated electrolyte shows conspicuous stability towards both the Li-metal anode and high-voltage electrodes compared to all reported electrolytes, including concentrated ether and FEC-containing carbonate electrolytes.

Li-metal anode morphology

After 100 cycles, the Li surface in LiPF$_6$–EC/DMC shows substantial cracking and dendritic growth (Fig. 2a–c), where needle-like crystals with nano-to-micrometre high aspect ratios generate thick and highly porous Li depositions. This morphology is caused by continuous reactions between the Li metal and electrolyte, as evidenced by a low Coulombic efficiency (<80%) and poor cycling stability. Replacing EC by FEC reduces the porosity of deposited Li and the thickness of the cycled Li from 341 μm (blue line in Fig. 2c) to 290 μm. However, the remaining porous structures and cracking still overwhelm the Li-metal surface (Fig. 2d–f). In sharp contrast, in all-fluorinated electrolytes, the Li metal maintains a dense and smooth surface, with non-dendritic Li mounds ~10 μm in diameter (Fig. 2g–i and Supplementary Fig. 8). The thickness of the cycled Li metal was 266 μm after 100 cycles. This dense Li deposition has three advantages: (1) higher safety, because the mound-like Li morphology will be less likely to be able to penetrate separators; (2) higher Coulombic efficiency, indicating much lower Li and electrolyte consumption; and (3) higher volumetric capacity, simply because of the much denser Li packing. As Supplementary Fig. 9 shows, when the porosity is >65%, the Li metal becomes inferior to graphite in terms of volumetric capacity, which would eliminate the commercial viability of LMBs. After 100 cycles, the Li porosity cycled in EC/DMC

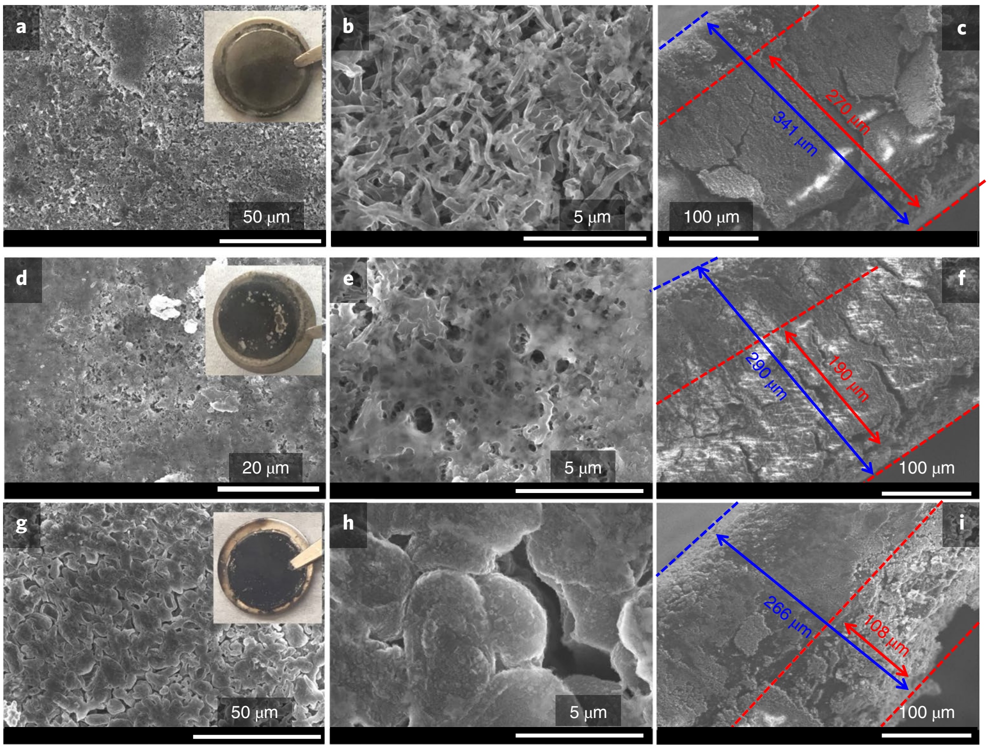

Fig. 2 | Scanning electron microscopy of Li-metal morphology after 100 cycles in different electrolytes at a current density of 0.5 mA cm^{-2}. a–i, Images after 100 cycles in 1 M LiPF$_6$ in EC/DMC (**a**–**c**), 1 M LiPF$_6$ in DMC/FEC (DMC:FEC = 8:2) (**d**–**f**) and 1 M LiPF$_6$ FEC/FEMC/HFE (FEC: FEMC:HFE = 2:6:2) (**g**–**i**). Insets in **a**, **d** and **g** show optical images of Li foils after cycling. The pristine Li metal thickness is 250 μm. In **c**, **f** and **i**, blue lines indicate the thickness of the Li metal cycled in different electrolytes, and red lines show the etching depth.

increased by 36%, while only a slight increase of 6% was observed with the all-fluorinated electrolyte (Supplementary Fig. 10).

The dense Li morphology with the all-fluorinated electrolyte was quantitatively confirmed by mapping the fluorine distribution through the depth of cycled Li metal (Supplementary Fig. 11). Because the fluorine species is generated by reaction between the Li metal and the electrolyte, its distribution in the cycled Li metal reflects the depth of etching by the electrolyte. Almost all the fluorine was found to reside within 1 μm distance of the top of the Li if cycled in all-fluorinated electrolyte, indicating a thin and robust LiF-rich layer that prevents the reaction of electrolyte with the underneath Li. However, Li cycled in EC/DMC exhibits a much lower fluorine content, with an even distribution throughout its thickness (>15 μm), a clear indication of a porous structure. This porous Li immediately collapsed during an attempted sputtering process (Supplementary Fig. 11a), revealing its mechanical fragility and its poor resistance towards chemical/electrochemical etching.

Electrochemical performance of Li-metal full cells

LMB full cells were constructed using aggressive cathodes NMC811 and LCP in various electrolytes with a high areal capacity (~2.0 mAh cm^{-2}). This loading presents a rigorous test for electrolyte stability, because it requires high Li-metal utilization and maximizes the parasitic reactions in each cycle. Meanwhile, the high voltages and highly catalytic surface of these cathodes also present a further challenge to the anodic stability of electrolytes[30]. All Li||NMC811 cells in the three different electrolytes exhibited similar initial lithiation/delithiation profiles with a specific capacity of 200 mAh g^{-1} (Fig. 3a)[31,32]. The all-fluorinated electrolyte presents the best cycling stability (Fig. 3b,c and Supplementary Fig. 12), retaining 90% of the original reversible capacity after 450 cycles, with an average Coulombic efficiency of ~99.93% (Supplementary Fig. 13), in comparison with <20% capacity retention for EC/DMC within 200 cycles (Fig. 3c and Supplementary Fig. 12a). Though FEC mitigates capacity fading, the Li||NMC811 still quickly decays in FEC/DMC to ~50% of the original capacity after 300 cycles (Fig. 3c and Supplementary Fig. 12b). The capacity decay mechanism was investigated by electrochemical impedance spectroscopy (EIS; Supplementary Fig. 14), where the semicircle in the high-frequency region is designated as the bulk electrolyte resistance R_e, and the other two are the interfacial resistances $R_{\mathrm{int1}} + R_{\mathrm{int2}}$ of the Li anode and NMC811 cathode. Both resistances, R_e and ($R_{\mathrm{int1}} + R_{\mathrm{int2}}$), increase from the 5th to 100th cycles in the following order: FEC/FEMC/HFE < FEC/DMC < EC/DMC (Supplementary Table 1). The largest increase in R_e (129%) occurs for EC/DMC due to the continuous consumption of electrolyte at both the Li-metal and cathode surfaces within 100 cycles; the accompanying quick increase in ($R_{\mathrm{int1}} + R_{\mathrm{int2}}$) (463%) is due to the continuous SEI growth. In contrast, the increases in both R_e and ($R_{\mathrm{int1}} + R_{\mathrm{int2}}$) in the all-fluorinated electrolyte are only 92% and 67%, respectively. In addition to cycling stability, the Li||NMC811 cell in all-fluorinated electrolyte also exhibits promising rate capability (Supplementary Fig. 15). A reversible capacity of 170 mAh g^{-1} can still be delivered at a 2C rate. A more rigorous cycling stability test for LMBs was performed with a Li-free Cu||NMC811 cell, where all cyclable Li comes from the lithiated cathode (Supplementary Fig. 16). The cells with all-fluorinated electrolyte retained a capacity of 78 mAh g^{-1} after 30 cycles, 60 times higher than that of cells in EC/DMC electrolyte.

Though the highly dense, electronically insulated F-rich CEI formed in situ by the all-fluorinated electrolyte stabilizes NMC811, possible intermixing of Li and Ni with O evolution during cycling could still occur and be responsible for capacity fade. To eliminate this factor, we constructed a 5.0 V LMB with LCP as the cathode, as this has higher structure stability than NMC811, despite its

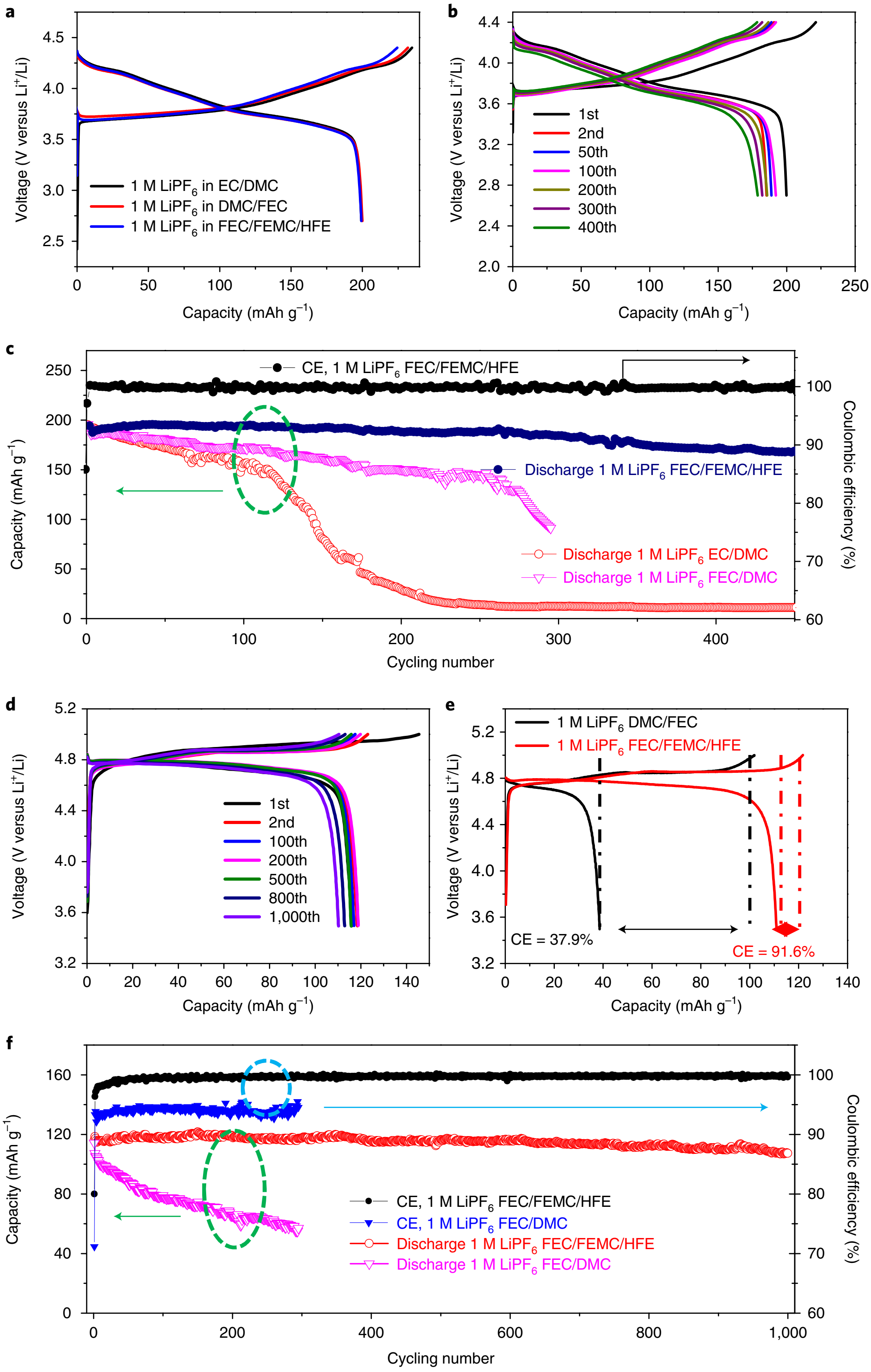

Fig. 3 | Electrochemical performances of LMBs using NMC811 and LCP as cathode materials. a, Initial galvanostatic charge–discharge curves of Li||NMC811 cells in different electrolytes at C/4. **b**, Galvanostatic charge–discharge curves of Li||NMC811 batteries using 1 M $LiPF_6$ FEC/FEMC/HFE electrolyte. **c**, Cycling stability of Li||NMC811 cells in different electrolytes when cycled at 0.5C, and charge–discharge profiles of Li||LCP batteries during different cycles using 1 M $LiPF_6$ FEC/FEMC/HFE electrolyte. CE, Coulombic efficiency. **d**, Recoverable capacity from fully charged Li||LCP cells in different electrolytes after resting for 48 h. **e**,**f**, Cycling stability of Li||LCP cells using FEC/DMC and 1 M $LiPF_6$ FEC/FEMC/HFE electrolyte when cycled at 1C.

higher operating potential (5.0 V). It has been reported that LCP can be charged–discharged reversibly in EC/DMC for only tens of cycles with a low Coulombic efficiency of 94–97%[33–35]. Though FEC enhanced the cycling stability, the capacity still quickly dropped to 60% of the original value after 300 cycles (Fig. 3f and Supplementary Fig. 17), consistent with previous reports[35]. In sharp contrast, the

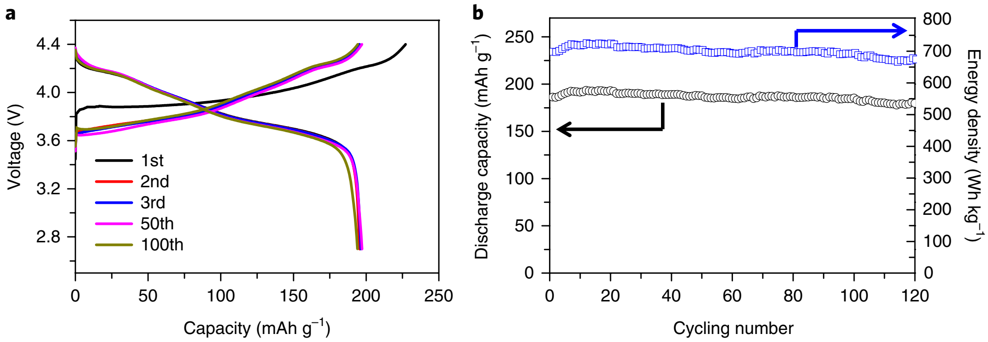

Fig. 4 | Electrochemical performance of Li||NMC811 batteries (with onefold Li excess) using 1 M LiPF$_6$ FEC/FEMC/HFE electrolyte. **a**, Charge–discharge curves. **b**, Cycling capacity and energy density. Capacity and energy density are calculated based on total masses of cathode (NMC811) and anode (onefold Li excess).

all-fluorinated electrolyte led to stable Li||LCP cells, as evidenced by a 93% capacity retention after 1,000 cycles (Fig. 3d,f), and a record-high Coulombic efficiency of 99.81% (Fig. 3f) even as the cells were charged to 5.0 V. The cycling performance of high-voltage batteries has often been demonstrated at high C rates in previous reports, so that parasitic reactions can be minimized. To assess the stability of the electrolytes on the LCP surface more rigorously, we charged the cells to 5 V and kept them at open circuit for 48 h, then measured the recoverable capacity (Fig. 3e). The all-fluorinated electrolyte demonstrated a capacity retention more than 2.5 times higher than that observed for FEC/DMC. When the test was conducted at 60 °C, more pronounced stabilization was observed, with a capacity retention more than 7.5 times higher than FEC/DMC (Supplementary Fig. 18), further confirming its stability against oxidation at high voltage.

Given the high Coulombic efficiency of the Li metal (99.2%) and high oxidation stability, our all-fluorinated formulation could be regarded as an appealing electrolyte for LMB applications with other cathode chemistries. Figure 4 demonstrates the cycling behaviour of a Li||NMC811 cell with onefold Li excess, which demonstrates a stable cycling performance without capacity decay for more than 120 cycles. A high energy density of >680 Wh kg^{-1} based on the total cathode/anode masses is achieved. Though the Li metal was depleted after 125 cycles in this cell, and the reversible capacity began to decay as in an anode-free battery (Supplementary Fig. 19), this battery still has the highest energy density among LMBs because of the minimized Li metal excess and the high energy of the cathode.

Chemistry at the interphase

Drastic differences in stability are observed between the three electrolytes on both the Li-metal and high-voltage cathode surfaces because of the solvent compositions. The most significant difference in these electrolyte formulations lies in their fluorine content, 22 M for the all-fluorinated electrolyte, 1.8 M for FEC/DMC and 0 M for EC/DMC (Supplementary Fig. 20). This fluorine content eventually affects the composition and robustness of the respective interphases. Quantum chemistry calculations predict LiF formation as a result of defluorination of the solvent bound to the Li$^+$ and LiPF$_6$ ion pairs (Fig. 5a, Supplementary Figs. 21 and 22 and Supplementary Note 1). Polarization of carbon cloth at 1.6 V in the all-fluorinated electrolyte confirmed these predictions (Supplementary Fig. 23)[36,37]. X-ray photoelectron spectroscopy (XPS) was used to identify both the SEI (Fig. 5d–f and Supplementary Figs. 24–27) and CEI components (Fig. 5g and Supplementary Figs. 28–30). In C1*s* spectra, carbonyl species at ~289.0 eV, ethereal carbon at ~286.5 eV and hydrocarbon at ~285.0 eV were detected for the SEI formed in EC/DMC (Supplementary Figs. 24–26), along with LiF, Li_2O and PO_xF_y arising either from salt anion or trace contaminates, which agrees with previous reports[13,15,18,38]. The evolution of the selected elements with depth profiling (Fig. 5d) reveals that the SEI originating from EC/DMC is characterized by a distinctly low fluorine but rather high organic content. LiF significantly increases as EC is replaced by FEC (>60%, Fig. 5e). Meanwhile, the C–C/C–H species gradually reduce with surface thickness. This LiF-rich SEI stabilizes the Li metal[39]. When the electrolyte becomes 'all fluorinated', with each co-solvent being a potential F donor, an extremely high LiF content (~90%) was detected, which increases with SEI depth (Fig. 5f) and indicates a more uniform interphase. LiF plays two critical roles here: (1) being a good electronic insulator and blocking electron tunnelling through the SEI[40], which has been the main cause for continuous electrolyte consumption and capacity loss[41]; (2) presenting high interfacial energy to the Li metal[7], which promotes Li$^+$ migration along the interface and encourages growth of the deposited Li metal in a parallel rather than vertical direction with regard to the electrode plane. This preferential alignment of Li-metal crystallization further reduces the specific surface area, minimizes parasitic reactions between the electrolyte and Li metal, and suppresses dendritic growth[42].

Unlike for the SEI, CEI formation involves not only electrolyte but also active components in the cathodes; this includes transition metal dissolution, solvent H abstraction and O-layer reaction into super-oxides or peroxides. For unmodified NMC811 or LCP cathodes, electrolyte components experience sustained oxidation until a CEI forms and blocks electron transfer from the electrolyte to the cathodes[5]. Compared with EC/DMC and FEC/DMC electrolytes, the extremely high Coulombic efficiencies achieved by the all-fluorinated electrolyte on aggressive cathodes should originate from the F-rich CEI that deactivates the catalytic activity of the NMC or LCP surfaces. Quantum chemistry calculations (Supplementary Note 2) predict that direct oxidation of solvent molecules is energetically unfavourable around 5 V. Instead, solvent oxidation is accompanied by H transfer to another solvent (Supplementary Fig. 31) and/or cathode surface. Intermolecular H transfer occurs around 5 V for EC and >5.5 V for FEC, FEMC and HFE (Supplementary Table 2). When the oxidation potential is calculated assuming open $EC^{\bullet}_{(\text{-H})}$ and $FEC^{\bullet}_{(\text{-H})}$ radicals as products, the oxidation stability decreased to ~4.2 and 4.9 V for EC and FEC, respectively. Thus, EC-containing electrolytes are expected to begin to be oxidized at 4.2 V (Fig. 1d), even in the absence of the active cathode surface. Density functional theory (DFT) calculations (Fig. 6) show that, for the fully charged $CoPO_4$ cathode, H transfer occurs for all solvents, with reaction energies being the most favourable for EC (Fig. 6e) and the least favourable for HFE (Fig. 6h). EC also dissociates on the $Ni_{0.5}Mn_{1.5}O_4$ (ref. [43]), $Li_xMn_2O_4$ (ref. [44]) or layered oxide cathode surfaces[45]. EC is a poor CEI former because the $EC^{\bullet}_{(\text{-H})}$ radical decomposes with a barrier of only 0.91 eV to evolve CO_2, leaving only a fraction of $EC^{\bullet}_{(\text{-H})}$

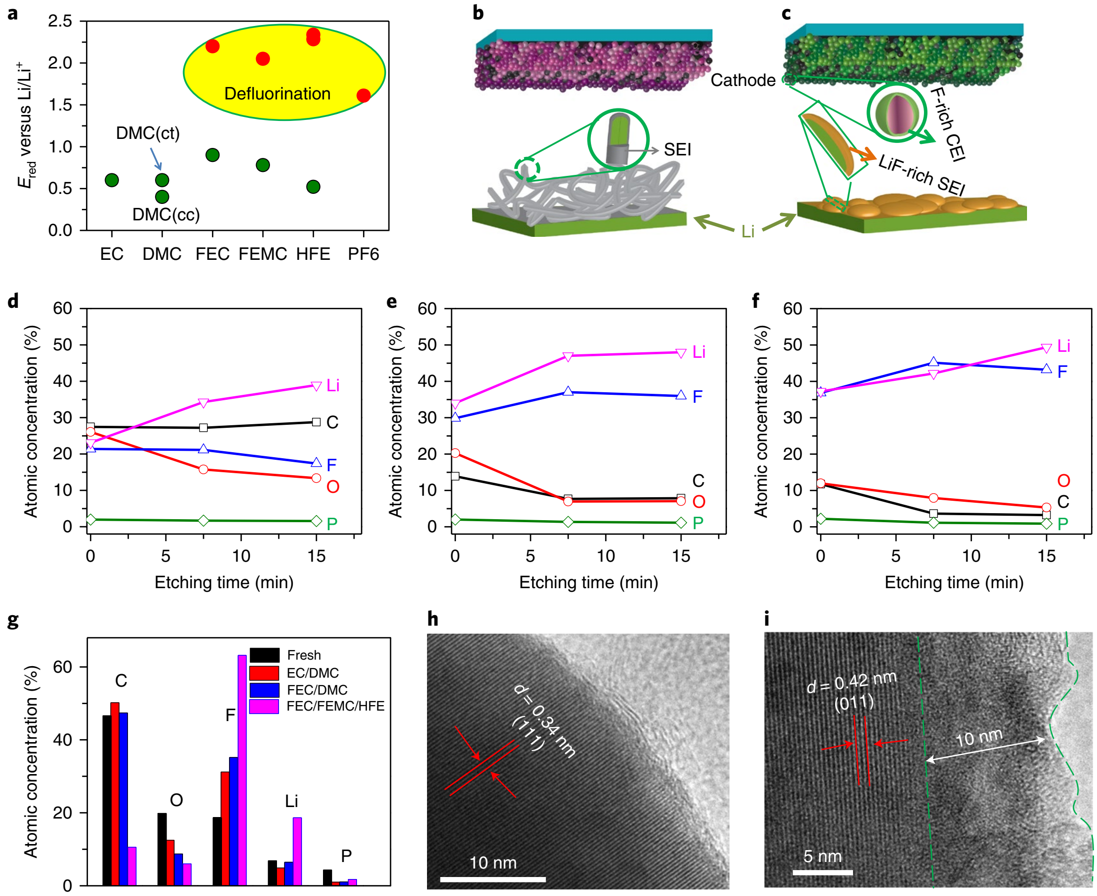

Fig. 5 | Calculated reduction/oxidation stability of electrolyte solvents and surface analyses performed on cycled Li-metal anode and LCP cathodes. **a**, Reduction potentials of Li$^+$(solvent)$_n$ and LiPF$_6$ from G4MP2 calculations with the SMD ($\varepsilon = 20$) implicit solvent model; data for LiPF$_6$, EC, FEC and DMC from ref. [50]. **b**,**c**, Variation of SEI and CEI chemistries formed in different electrolytes: traditional carbonate (**b**) and all-fluorinated (**c**). **d**–**f**, Composition of SEI after various durations of Ar$^+$ sputtering on Li metal cycled in 1 M LiPF$_6$-EC/DMC (**d**), 1 M LiPF$_6$-DMC/FEC (**e**) and 1 M LiPF$_6$ in FEC/FEMC/HFE (**f**). **g**, Composition of CEI on the cycled LCP cathode materials in different electrolytes. **h**,**i**, High-resolution transmission electron microscopy (HRTEM) images of fresh LCP (**h**) and LCP cycled in 1 M LiPF$_6$ FEC/FEMC/HFE electrolyte (**i**). ct, cis-trans; cc, cis-cis.

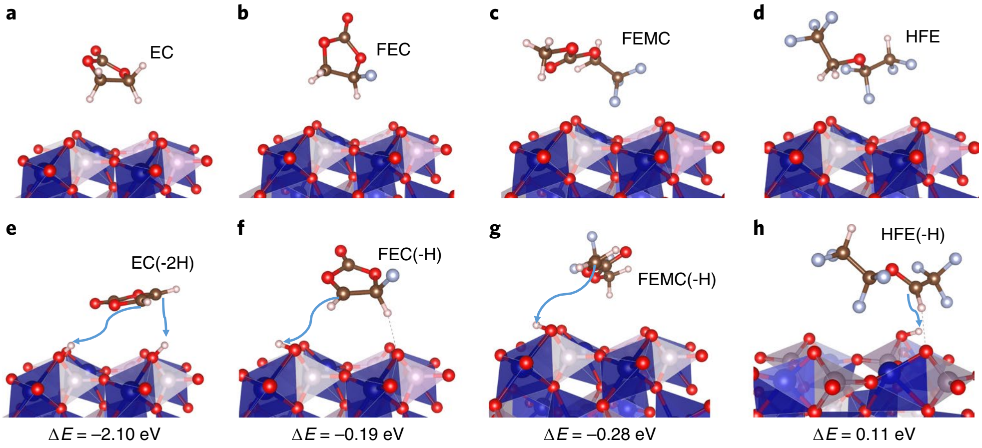

Fig. 6 | Reactivity of EC, FEC, FEMC and HFE solvents at the fully charged CoPO$_4$ (010) surface from PBE + U DFT calculations. **a**–**h**, Initial (**a**–**d**) and final (**e**–**h**) configurations and reaction energies. Arrows indicate H transfer reaction from solvent to surface oxygen. O, red; C, brown; F, light blue; H, white. CoPO$_4$ surfaces show PO$_4$ tetrahedron and CoO$_6$ octahedron connected with a PO$_4$ tetrahedron. ΔE, the energy difference between the physisorbed solvent molecule and the reacted solvent.

radicals to participate in the second H abstraction, eventually leading to polymerization, while the resulting hydrogen-rich polymer is still susceptible to further degradation. Because of the higher barrier (1.28 eV) for FEC$^\bullet_{(\text{-H})}$ ring opening compared to the EC$_{\bullet(\text{-H})}$, FEC$^\bullet_{(\text{-H})}$ is a longer-lived radical compared to EC$^\bullet_{(\text{-H})}$ (Fig. 6f), and will probably react with the FEMC$^\bullet_{(\text{-H})}$ (Fig. 6g) and HFE$^\bullet_{(\text{-H})}$ (Fig. 6h) radicals formed near the cathode surface, resulting in a fluorine-rich CEI as observed by Fourier-transform infrared spectroscopy (Supplementary Fig. 32). Alternatively, fluorinated radicals also bind to oxygen in $CoPO_4$ (Supplementary Fig. 33), preventing the OH formation that facilitates transition metal dissolution[46]. Thus, in the all-fluorinated electrolyte, a protective CEI is highly likely, the composition of which is inevitably highly fluorinated.

XPS confirmed the significantly high F contents in the CEI formed by the all-fluorinated electrolyte on LCP (Fig. 5g and Supplementary Figs. 28, 29 and 34), supported by a F/O ratio of 10.7, in strong contrast with the values of 2.4 for EC/DMC and 4.0 for FEC/DMC. Thermodynamically, these fluorine-containing species (CF_x and PO_xF_y species) are much more resistant to oxidation than oxide species, and their presence on the cathode surface constitutes a conformal and dense CEI that effectively suppresses the parasitic reactions between cathode and electrolyte[15]. Similar CEI compositions were also detected on cycled NMC811 (Supplementary Fig. 30). An amorphous layer (5–10 nm) was observed on the surfaces of both LCP (Fig. 5h,i) and NMC811 (Supplementary Fig. 35) after cycling in all-fluorinated electrolyte.

Besides the unique electrochemical benefits contributed by this all-fluorinated formulation, one additional advantage is non-flammability, which is highly desirable but often unavailable from non-aqueous electrolytes. As demonstrated in flaming tests (Supplementary Fig. 36 and Supplementary Videos 2, 3 and 4), this electrolyte does not burn following ignition, in sharp contrast with the highly flammable EC/DMC or the flame-retarded but still combustible DMC/FEC. This is attributed to the fluorine substitution on the alkyl moiety, which effectively serves as an inhibitor to the propagation of oxygen radicals during combustion[47,48]. Among the present cathode materials, the tendency of the delithiated NMC811 to release the atomic state of oxygen, which would oxidize organic solvents at a relatively low temperature, is known[49]. The resistance of EC/DMC and FEC/FEMC/HFE against such oxidation was evaluated by differential scanning calorimetry (DSC, Supplementary Fig. 37), where the delithiated NMC811 was heated in the presence of the electrolytes. The major exothermic peak indicates that such oxidation occurs at a much higher temperature for the all-fluorinated electrolyte. The combination of superior thermal stability and non-flammability of the all-fluorinated electrolyte render LMBs much safer.

Conclusions

In this work a non-flammable all-fluorinated electrolyte has been developed for the aggressive battery chemistries using a Li-metal anode and high-capacity/high-voltage cathodes. This electrolyte simultaneously solves the four most pressing challenges faced by such high-energy batteries: (1) poor Li plating/stripping; (2) electrolyte oxidation on delithiated cathode surfaces; (3) Li-dendrite formation; (4) poor safety. The two cathode chemistries selected in this work (NMC811, LCP) are only representative, chosen because of their advantageous properties (high capacity with strongly catalysing Ni-rich surface, and unusually high voltage), and the concept of interphase fluorination we show in the present work should be universally applicable to other battery chemistries such as Na-metal. In fact, significant increases in Na plating/stripping and improvement in oxidation stability are also observed (Supplementary Fig. 38). Our findings provide an alternative avenue (which we believe is more practical) to the high salt concentration approach for the design of new electrolyte systems for the most aggressive cathode and metal anode chemistries.

Methods

Methods, including statements of data availability and any associated accession codes and references, are available at https://doi.org/10.1038/s41565-018-0183-2.

Received: 6 January 2018; Accepted: 1 June 2018;

References

1. Armand, M. & Tarascon, J. M. Building better batteries. *Nature* **451**, 652–657 (2008).
2. Dunn, B., Kamath, H. & Tarascon, J. M. Electrical energy storage for the grid: a battery of choices. *Science* **334**, 928–935 (2011).
3. Etacheri, V., Marom, R., Elazari, R., Salitra, G. & Aurbach, D. Challenges in the development of advanced Li-ion batteries: a review. *Energy Environ. Sci.* **4**, 3243–3262 (2011).
4. Choi, J. W. & Aurbach, D. Promise and reality of post-lithium-ion batteries with high energy densities. *Nat. Rev. Mater.* **1**, 16013 (2016).
5. Goodenough, J. B. & Kim, Y. Challenges for rechargeable Li batteries. *Chem. Mater.* **22**, 587–603 (2009).
6. Lin, D., Liu, Y. & Cui, Y. Reviving the lithium metal anode for high-energy batteries. *Nat. Nanotech.* **12**, 194–206 (2017).
7. Lu, Y., Tu, Z. & Archer, L. A. Stable lithium electrodeposition in liquid and nanoporous solid electrolytes. *Nat. Mater.* **13**, 961–969 (2014).
8. Choudhury, S., Mangal, R., Agrawal, A. & Archer, L. A. A highly reversible room-temperature lithium metal battery based on crosslinked hairy nanoparticles. *Nat. Commun.* **6**, 10101 (2015).
9. Aurbach, D., Zinigrad, E., Cohen, Y. & Teller, H. A short review of failure mechanisms of lithium metal and lithiated graphite anodes in liquid electrolyte solutions. *Solid State Ion.* **148**, 405–416 (2002).
10. Ding, F. et al. Effects of carbonate solvents and lithium salts on morphology and Coulombic efficiency of lithium electrode. *J. Electrochem. Soc.* **160**, A1894–A1901 (2013).
11. Jeong, S. K. et al. Suppression of dendritic lithium formation by using concentrated electrolyte solutions. *Electrochem. Commun.* **10**, 635–638 (2008).
12. Xu, W. et al. Lithium metal anodes for rechargeable batteries. *Energy Environ. Sci.* **7**, 513–537 (2014).
13. Xu, K. Nonaqueous liquid electrolytes for lithium-based rechargeable batteries. *Chem. Rev.* **104**, 4303–4418 (2004).
14. Li, W. et al. The synergetic effect of lithium polysulfide and lithium nitrate to prevent lithium dendrite growth. *Nat. Commun.* **6**, 7436 (2015).
15. Xu, K. Electrolytes and interphases in Li-ion batteries and beyond. *Chem. Rev.* **114**, 11503–11618 (2014).
16. Qian, J. et al. High rate and stable cycling of lithium metal anode. *Nat. Commun.* **6**, 6362 (2015).
17. Cheng, X. B. et al. Dendrite-free lithium deposition induced by uniformly distributed lithium-ions for efficient lithium metal batteries. *Adv. Mater.* **28**, 2888–2895 (2016).
18. Erickson, E. M. et al. Review—development of advanced rechargeable batteries: a continuous challenge in the choice of suitable electrolyte solutions. *J. Electrochem. Soc.* **162**, A2424–A2438 (2015).
19. Li, J., Downie, L. E., Ma, L., Qiu, W. & Dahn, J. R. Study of the failure mechanisms of $LiNi_{0.8}Mn_{0.1}Co_{0.1}O_2$ cathode material for lithium ion batteries. *J. Electrochem. Soc.* **162**, A1401–A1408 (2015).
20. Ma, J., Hu, P., Cui, G. & Chen, L. Surface and interface issues in spinel $LiNi_{0.5}Mn_{1.5}O_4$: insights into a potential cathode material for high energy density lithium ion batteries. *Chem. Mater.* **28**, 3578–3606 (2016).
21. Arumugam, R. S. et al. Special synergy between electrolyte additives and positive electrode surface coating to enhance the performance of $Li[Ni_{0.6}Mn_{0.2}Co_{0.2}]O_2$/graphite cells. *J. Electrochem. Soc.* **163**, A2531–A2538 (2016).
22. Bramnik, N. N., Nikolowski, K., Baehtz, C. K., Bramnik, G. & Ehrenberg, H. Phase transitions occurring upon lithium insertion–extraction of $LiCoPO_4$. *Chem. Mater.* **19**, 908–915 (2007).
23. Duncan, H., Abu-Lebdeh, Y. & Davidson, I. J. Study of the cathode–electrolyte interface of $LiMn_{1.5}Ni_{0.5}O_4$ synthesized by a sol–gel method for Li-ion batteries. *J. Electrochem. Soc.* **157**, A528–A535 (2010).
24. Zhang, X. Q., Cheng, X. B., Chen, X., Yan, C. & Zhang, Q. Fluoroethylene carbonate additives to render uniform Li deposits in lithium metal batteries. *Adv. Funct. Mater.* **27**, 1605989 (2017).
25. Fan, X. et al. Highly fluorinated interphases enable high-voltage Li-metal batteries. *Chem* **4**, 174–185 (2018).
26. Suo, L. et al. Fluorine-donating electrolytes enable highly reversible 5-V-class Li metal batteries. *Proc. Natl Acad. Sci. USA* **115**, 1156–1161 (2018).
27. Wang, J. et al. Fire-extinguishing organic electrolytes for safe batteries. *Nat. Energy* **3**, 22–29 (2018).
28. Zhang, Z. et al. Fluorinated electrolytes for 5 V lithium-ion battery chemistry. *Energy Environ. Sci.* **6**, 1806–1810 (2013).
29. Xia, J. et al. Fluorinated electrolyte for 4.5 V $Li(Ni_{0.4}Mn_{0.4}Co_{0.2})O_2$/graphite Li-ion cells. *J. Power Sources* **307**, 340–350 (2016).
30. Li, J. et al. The impact of electrolyte additives and upper cut-off voltage on the formation of a rocksalt surface layer in $LiNi_{0.8}Mn_{0.1}Co_{0.1}O_2$ electrodes. *J. Electrochem. Soc.* **164**, A655–A665 (2017).
31. Liu, W. et al. Nickel-rich layered lithium transition-metal oxide for high-energy lithium-ion batteries. *Angew. Chem. Int. Ed.* **54**, 4440–4457 (2015).

32. Myung, S. T. et al. Nickel-rich layered cathode materials for automotive lithium-ion batteries: achievements and perspectives. *ACS Energy Lett.* **2**, 196–223 (2017).
33. Wolfenstine, J., Lee, U., Poese, B. & Allen, J. L. Effect of oxygen partial pressure on the discharge capacity of $LiCoPO_4$. *J. Power Sources* **144**, 226–230 (2005).
34. Liu, J. et al. Spherical nanoporous $LiCoPO_4$/C composites as high performance cathode materials for rechargeable lithium-ion batteries. *J. Mater. Chem.* **21**, 9984–9987 (2011).
35. Sharabi, R. et al. Electrolyte solution for the improved cycling performance of $LiCoPO_4$/C composite cathodes. *Electrochem. Commun.* **28**, 20–23 (2013).
36. Leung, K., Soto, F., Hankins, K., Balbuena, P. B. & Harrison, K. L. Stability of solid electrolyte interphase components on lithium metal and reactive anode material surfaces. *J. Phys. Chem. C* **120**, 6302–6313 (2016).
37. Tasaki, K. et al. Solubility of lithium salts formed on the lithium-ion battery negative electrode surface in organic solvents. *J. Electrochem. Soc.* **156**, A1019–A1027 (2009).
38. Cheng, X. B. et al. A review of solid electrolyte interphases on lithium metal anode. *Adv. Sci.* **3**, 1500213 (2015).
39. Markevich, E., Salitra, G., Chesneau, F., Schmidt, M. & Aurbach, D. Very stable lithium metal stripping–plating at a high rate and high areal capacity in fluoroethylene carbonate-based organic electrolyte solution. *ACS Energy Lett.* **2**, 1321–1326 (2017).
40. Zhang, Q. et al. Synergetic effects of inorganic components in solid electrolyte interphase on high cycle efficiency of lithium ion batteries. *Nano Lett.* **16**, 2011–2016 (2016).
41. Leung, K. Electronic structure modeling of electrochemical reactions at electrode/electrolyte interfaces in lithium ion batteries. *J. Phys. Chem. C* **117**, 1539–1547 (2013).
42. Liu, Z. et al. Interfacial study on solid electrolyte interphase at Li metal anode: implication for Li dendrite growth. *J. Electrochem. Soc.* **163**, A592–A598 (2016).
43. Borodin, O., Olguin, M., Spear, C. E., Leiter, K. & Knap, J. Towards high throughput screening of electrochemical stability of battery electrolytes. *Nanotechnology* **26**, 354003 (2015).
44. Kumar, N., Leung, K. & Siegel, D. J. Crystal surface and state of charge dependencies of electrolyte decomposition on $LiMn_2O_4$ cathode. *J. Electrochem. Soc.* **161**, E3059–E3065 (2014).
45. Giordano, L. et al. Chemical reactivity descriptor for the oxide–electrolyte interface in Li-ion batteries. *J. Phys. Chem. Lett.* **8**, 3881–3887 (2017).
46. Leung, K. First-principles modeling of Mn(ii) migration above and dissolution from $Li_xMn_2O_4$ (001) surfaces. *Chem. Mater.* **29**, 2550–2562 (2017).
47. Xu, K., Zhang, S., Allen, J. L. & Jow, T. R. Nonflammable electrolytes for Li-ion batteries based on a fluorinated phosphate. *J. Electrochem. Soc.* **149**, A1079–A1082 (2002).
48. Nagasubramanian, G. & Orendorff, C. J. Hydrofluoroether electrolytes for lithium-ion batteries: reduced gas decomposition and nonflammable. *J. Power Sources* **196**, 8604–8609 (2011).
49. Sun, Y. K. et al. Nanostructured high-energy cathode materials for advanced lithium batteries. *Nat. Mater.* **11**, 942–947 (2012).
50. Delp, S. A. et al. Importance of reduction and oxidation stability of high voltage electrolytes and additives. *Electrochim. Acta* **209**, 498–510 (2016).

Acknowledgements

This work was supported by the US Department of Energy (DOE) under award no. DEEE0008202 and DEEE0008200. The support of the Maryland NanoCenter and its AIM Lab is acknowledged. The authors thank K. Pupek and G. Krumdick for providing one of the fluorinated solvents, and B. Dunn for constructive discussions.

Author contributions

X.F. and L.C designed the experiments and analysed data. O.B. conducted the calculations. X.F., L.C., X.J., J.C., S.H., T.D., J.Z. and C.Y. conducted electrochemical experiments. X.F. and S.-C.L. performed the TEM analysis. K.A., K.X. and C.W. conceived and supervised the project. All authors contributed to interpretation of the results.

Competing interests

The authors declare no competing interests.

Additional information

Supplementary information is available for this paper at https://doi.org/10.1038/s41565-018-0183-2.

Reprints and permissions information is available at www.nature.com/reprints.

Correspondence and requests for materials should be addressed to K.A. or K.X. or C.W.

Publisher's note: Springer Nature remains neutral with regard to jurisdictional claims in published maps and institutional affiliations.

Methods

Materials. Li chips with a thickness of 250 µm were purchased from MTI Corporation. Cathode NMC811 ($LiNi_{0.8}Mn_{0.1}Co_{0.1}O_2$) electrode laminates (~10.8 mg cathode material per cm^2) were obtained from Argon National Lab. The electrode was cut into discs and dried at 80 °C under vacuum overnight. Dimethyl carbonate (DMC), fluoroethylene carbonate (FEC), ethylene carbonate (EC) and propylene carbonate (PC) were bought from Sigma-Aldrich. 1,1,2,2-tetrafluoroethyl-2′,2′,2′-trifluoroethyl (HFE) was purchased from SynQuest and dried over activated molecular sieves before use. Methyl (2,2,2-trifluoroethyl) carbonate (FEMC) was synthesized at the Materials Engineering Research Facility of Argonne National Lab and provided to Army Research Lab, where it was dried over activated molecular sieves before use. Cathode $LiCoPO_4$ was synthesized based on the literature[51]. Salts $LiPF_6$ (99.99%, BASF), $NaPF_6$ (>99%, Sigma-Aldrich), lithium bis(fluorosulfonyl) imide (LiFSI, 99.9%, BASF) and sodium bis(fluorosulfonyl)imide (NaFSI, 99.7%, Solvionic) were used as received.

Screening of electrolytes. The development of a new electrolyte formulation must often balance a series of conflicting requirements that cannot be achieved with a single solvent and salt. At least five major properties must be taken into account: (1) salt solubility; (2) ion conductivity; (3) wettability to both separator and electrodes; (4) stability against sustained reductive or oxidative decompositions; (5) ability to contribute desired interphase chemistry ingredients. To ensure that a highly fluorinated interphase with maximum protection power be formed, we sought an all-fluorinated electrolyte formulation in which all components (solvents, salt anion) that are likely to be involved in interphase formation chemistry must contain at least one fluorine in its structure. Assisted by DFT calculations, we identified a few solvents with varying fluorination degree that would probably lead to highly fluorinated interphases on both anode and cathode, and experiments further downselected their combinations to address the requirements of solubility, conductivity and wettability. The eventual optimized formulation consisted of 1.0 M $LiPF_6$ dissolved in a mixture of HFE, FEMC and FEC at a weight ratio of 2:6:2. As the most polar of all three solvents, FEC served as the main solvating agent, whose presence had to be 20% to ensure sufficient salt concentration, while FEMC and HFE both served as diluents to increase ion conductivity. According to the DFT calculations, the HFE component had the highest oxidation stability and produced the most LiF per solvent molecule during reduction (because of its high F density).

According to DFT calculations, the HFE component has the highest oxidation stability and produced the most LiF per solvent molecule during reduction; however, its salt solubility and conductivity are limited, requiring the presence of FEC and FEMC. The former has the highest dielectric constant and highest affinity to Li$^+$ (Supplementary Fig. 23) of the three solvents, and is mainly responsible for $LiPF_6$ dissociation (Supplementary Fig. 39). Because of its smallest F content, $FEC^{\bullet}_{(\text{-H})}$ ring opening could still induce some gas generation reaction, though this reaction is slow. Therefore, FEC composition should be low but sufficient for ionic conductivity.

Material characterization. The Li-metal morphology was characterized by scanning electron microscopy (Hitachi SU-70 FEG SEM). TEM images were obtained with a JEOL JEM 2100 LaB_6 transmission electron microscope with an electron accelerating voltage of 200 keV. XPS data were collected using a high-sensitivity X-ray photoelectron spectrometer (Kratos AXIS 165, Mg Kα radiation). The C1*s* peak (284.6 eV) was utilized as the reference to calibrate other binding energy values. The electrodes were rinsed and dried under vacuum before characterizations. The contents of different species in the SEI and CEI layers were obtained by fitting the whole XPS spectra using CasaXPS software. The distribution of the constituent elements at different depths in the cycled Li metal was analysed using time-of-flight secondary ion mass spectroscopy (ToF-SIMS) attached to a Ga$^+$ focused-ion beam (FIB)/SEM (Tescan GAIA3) at an accelerated voltage of 20 kV and 1 nA current. DSC experiments were performed with a TA Q600 differential scanning calorimeter. The scanning rate was 5 °C min^{-1}. Before tests, the Li||NMC811 cells were charged to 4.4 V, and held for 1 h. The charged cell was then disassembled in a glove box. Charged NMC811 material (5 mg) was sealed with the electrolyte in a high-pressure DSC vessel (30 µl).

Electrochemical measurements. All cell assembling/disassembling, and electrolyte preparation, were performed in an Ar-filled glove box with moisture and O_2 content below 2 ppm. Before preparing the electrolytes, the solvents were dried over an activated molecular sieve (4 Å). A Karl Fisher titrater (Metrohm 899 Coulometer) was utilized to measure the water content of the electrolytes, which was lower than 10 ppm in all prepared electrolytes. Coin cells (2032 type) were used to test the electrochemical performance of the LMBs. The voltage window for the different electrolytes was tested using a three-electrode T-cell. Li metal was used as the counter and reference electrodes, and polished stainless steel was utilized as the working electrode. The charge/discharge properties of the cells were determined using an Arbin battery test station (BT2000, Arbin Instruments). For Li||NMC811, two activation cycles (C/4, 50 mA g^{-1}) were conducted before a long-term cycle-life test at a higher charge/discharge current (C/2). For the Li||NMC811 battery with onefold Li excess, the onefold excess Li electrode was pre-deposited on the current collector. Before deposition, the current collector was pre-cycled (plating/stripping) for 5 cycles to remove possible oxidation layers. Onefold excess means that the capacity ratio of the pre-deposited Li metal to cathode capacity is 1. The cathode areal capacity was 2 mAh cm^{-2}. Therefore, we pre-deposited Li metal on the current collector with an areal capacity of 2 mAh cm^{-2}. The same disc size was used for the cathode and anode. For the 2032 coin cell, the loading of the cathode was 2 mAh cm^{-2}. The disc area was 1.5 cm^2. The volume of the electrolyte in the coin cell was 100 µl. The electrolyte-soaked glass fibre filter was used to test the flammability of the electrolytes.

Methodology of quantum chemistry calculations. To provide insight into the initial reduction and oxidation reactions for the representative electrolyte model compounds, quantum chemistry calculations were performed. Two types of calculation were performed: (1) cluster calculations aimed at predicting the reduction and oxidation potentials of the representative electrolyte clusters and their initial decomposition reactions, using the Gaussian g09 rev. c package[52]; (2) solvent reactions with the charged $CoPO_4$ cathode surface, aimed at understanding the first step of electrolyte oxidation at the cathode surface, utilizing periodic plane-wave DFT approaches with Vienna ab initio Simulation Package (VASP) software package.

Cluster calculations. Solvent electrochemical stability versus Li$^+$/Li was predicted using quantum chemistry calculations by subtracting 1.4 V from the absolute oxidation and reduction potentials, as given in equations (1) and (2), respectively[53,54]:

$$E_{\mathrm{ox}}(\mathrm{M}) = [\Delta G_{\mathrm{e}} + \Delta G_{\mathrm{S}}^{0}(\mathrm{M}^{+}) - \Delta G_{\mathrm{S}}^{0}(\mathrm{M})] \ / \ F - 1.4\mathrm{V} \tag{1}$$

$$E_{\mathrm{red}}(\mathrm{M}) = -[\Delta G_{\mathrm{e}} + \Delta G_{\mathrm{S}}^{0}(\mathrm{M}^{-}) - \Delta G_{\mathrm{S}}^{0}(\mathrm{M})] \ / \ F - 1.4\mathrm{V} \tag{2}$$

In the equations, ΔG_e is the ionization free energy for equation (1) or electron affinity for equation (2) in the gas phase at room temperature (298.15 K), $\Delta G_S(M)$, $\Delta G_S(M^-)$ and $\Delta G_S(M^+)$ are the Gibbs free energies of solvation for the M, M$^-$ and M$^+$ complexes, respectively, and F is the Faraday constant[55]. It is believed that solvent variation will change the conversion factor of 1.4 V by 0.1–0.3 V, as previously discussed[53,56].

The composite G4MP2 methodology was used for quantum chemistry calculations on smaller clusters. It is more reliable than DFT methods for the abstraction reactions, but becomes computationally prohibitive for large systems[57,58]. For larger and intermediate size clusters the M05-2× density functional was adopted because it precisely predicts ionization potential, electron affinity[59] and yields a more realistic electron–hole localization in the oxidized ethylene carbonate than the popular B3LYP functional[60]. The SMD implicit solvation model[61] with acetone parameters and dielectric constant ($\varepsilon = 20.493$) was used to represent solvent molecules not explicitly included in quantum chemistry calculations.

Periodic calculations. Periodic plane-wave DFT calculations with Hubbard U correction were performed for the charged $CoPO_4$ cathode with EC, FEC, FEMC and HFE molecules adsorbed on the cathode surface. The projector augmented wave (PAW) scheme and spin-polarized Perdew–Burke–Ernzerhof exchange-correlation functional were used to treat core electrons[62–66] using the VASP package. An energy cutoff was set to be 400 eV. A 2 × 1 × 2 k-point sampling was adopted for the slab calculations. We followed previous work[67,68] for the +U augmented treatment of Co 3*d* orbitals and used a U_{eff} value of 6.7 eV and $J = 1.0$ eV. A $CoPO_4$ bulk crystal was optimized, then the (010) surface was created and optimized. The $CoPO_4$ slab contained 96 atoms. The (010) surface was previously found to be the lowest energy in DFT studies of $LiFePO_4$ and $FePO_4$ (ref. [69]). A low spin antiferromagnetic (AFM) ordering was used, in accord with previous studies[68]. The simulation cell dimensions were 10.10 Å × 30.73 Å × 9.394 Å that allowed two surfaces without adsorbents to be separated by 19 Å to ensure minimum interaction between the periodic images. EC, FEC, FEMC and HFE molecules were placed on the $CoPO_4$ surface in multiple orientations, with some of the H atoms pointing towards surface O atoms following previous studies for EC on fully and partially delithiated cathode surfaces[43,45]. Only the most stable configurations are shown Fig. 6. In a second set of calculations, one H atom from the solvent was transferred to the closest surface O, and the geometry was optimized again. During geometry optimization, all O atoms in the top surface were allowed to relax, while other atoms of the $CoPO_4$ were fixed. We set the energy convergence criteria to 10^{-5} or 10^{-6} eV A^{-1}, and forces were converged below 0.01 eV Å^{-2} during geometry optimization.

Data availability. The data that support the plots within this paper and other findings of this study are available from the corresponding authors upon reasonable request.

References

51. Allen, J. L., Jow, T. R. & Wolfenstine, J. Improved cycle life of Fe-substituted $LiCoPO_4$. *J. Power Sources* **196**, 8656–8661 (2011).
52. Frisch, M. J. et al. Gaussian 09, Revision C (Gaussian, Inc., 2010).
53. Borodin, O., Behl, W. & Jow, T. R. Oxidative stability and initial decomposition reactions of carbonate, sulfone, and alkyl phosphate-based electrolytes. *J. Phys. Chem. C* **117**, 8661–8682 (2013).
54. Borodin, O. in *Electrolytes for Lithium and Lithium-Ion Batteries* Vol. 58 (eds Jow, T. R. et al.) Ch. 8 (Springer, New York, NY, 2014).
55. Gomer, R. & Tryson, G. An experimental determination of absolute half-cell emf's and single ion free energies of solvation. *J. Chem. Phys.* **66**, 4413–4424 (1977).
56. Trasatti, S. The absolute electrode potential—an explanatory note (Recommendations 1986). *Pure Appl. Chem.* **58**, 955–966 (1986).
57. Lin, C. Y., Hodgson, J. L., Namazian, M. & Coote, M. L. Comparison of G3 and G4 theories for radical addition and abstraction reactions. *J. Phys. Chem. A* **113**, 3690–3697 (2009).
58. Curtiss, L. A., Redfern, P. C. & Raghavachari, K. G *n* theory. *WIRES Comput. Mol. Sci.* **1**, 810–825 (2011).
59. Zhao, Y. & Truhlar, D. G. The M06 suite of density functionals for main group thermochemistry, thermochemical kinetics, noncovalent interactions, excited states, and transition elements: two new functionals and systematic testing of four M06-class functionals and 12 other functionals. *Theor. Chem. Acc.* **120**, 215–241 (2008).
60. Barnes, T. A., Kaminski, J. W., Borodin, O. & Miller, T. F. Ab initio characterization of the electrochemical stability and solvation properties of condensed-phase ethylene carbonate and dimethyl carbonate mixtures. *J. Phys. Chem. C* **119**, 3865–3880 (2015).
61. Marenich, A. V., Cramer, C. J. & Truhlar, D. G. Universal solvation model based on solute electron density and on a continuum model of the solvent defined by the bulk dielectric constant and atomic surface tensions. *J. Phys. Chem. B* **113**, 6378–6396 (2009).
62. Kresse, G. & Furthmüller, J. Efficient iterative schemes for ab initio total-energy calculations using a plane-wave basis set. *Phys. Rev. B* **54**, 11169–11186 (1996).
63. Kresse, G. & Furthmuller, J. Efficiency of ab-initio total energy calculations for metals and semiconductors using a plane-wave basis set. *Comput. Mater. Sci.* **6**, 15–50 (1996).
64. Kresse, G. & Joubert, D. From ultrasoft pseudopotentials to the projector augmented-wave method. *Phys. Rev. B* **59**, 1758–1775 (1999).
65. Paier, J., Marsman, M. & Kresse, G. Why does the B3LYP hybrid functional fail for metals?. *J. Chem. Phys.* **127**, 024103 (2007).
66. Perdew, J. P., Burke, K. & Ernzerhof, M. Generalized gradient approximation made simple (vol. 77, p. 3865, 1996). *Phys. Rev. Lett.* **78**, 1396–1396 (1997).
67. Johannes, M., Hoang, D. K., Allen, J. L. & Gaskell, K. Hole polaron formation and migration in olivine phosphate materials. *Phys. Rev. B* **85**, 115106 (2012).
68. Zhou, F., Cococcioni, M., Marianetti, C. A., Morgan, D. & Ceder, G. First-principles prediction of redox potentials in transition-metal compounds with LDA+U. *Phys. Rev. B* **70**, 235121 (2004).
69. Wang, L., Zhou, F., Meng, Y. S. & Ceder, G. First-principles study of surface properties of $LiFePO_4$: surface energy, structure, Wulff shape, and surface redox potential. *Phys. Rev. B* **76**, 165435 (2007).